

Article

Origin of the Bleaching in Lower Cretaceous Continental Red Beds in the Uragen Zn–Pb Deposit, Xinjiang, NW China, and Its Implications for Zn–Pb Mineralization

Rongzhen Gao ¹ , Chunji Xue ^{2,*}, Junfeng Dai ³ and Ronghao Man ⁴

¹ Key Laboratory of Ministry of Education on Safe Mining of Deep Metal Mines, School of Resources and Civil Engineering, Northeastern University, Shenyang 110819, China; rongzhengao01@163.com

² State Key Laboratory of Geological Processes and Mineral Resource, School of Earth Sciences and Resources, China University of Geosciences, Beijing 100083, China

³ Key Laboratory on Nuclear Resources and Environment, East China University of Technology, Nanchang 330013, China; daijf90@163.com

⁴ Graduate School, Hebei GEO University, Shijiazhuang 050031, China; sandmrh@163.com

* Correspondence: chunji.xue@cugb.edu.cn; Tel.: +86-10-8232-1895

Abstract: The Uragen giant sandstone-hosted Zn–Pb deposit has a proven reserve of 5.90 Mt metals in the southern ore zone and potentially 10 Mt metals for the whole deposit, and orebodies are strictly confined to the bleached clastic rocks of the Lower Cretaceous red beds. The bleaching has been used to guide lead–zinc exploration; however, its nature and origin, as well as the relationship with Zn–Pb mineralization, remains unclear, although it is closely related to regional oil–gas infillings. Detailed field investigation and petrographic observation, TESCAN-integrated mineral analyzer (TIMA), and X-ray fluorescence (μ -XRF) analysis of the red and bleached sandstone at the same sedimentary layer demonstrate that the bleaching is mainly caused by the reductive dissolution of hematite pigment, which probably resulted from the interaction with H₂S formed by in situ sulfate reduction during hydrocarbon migration. The calcite cements in the bleached sandstones show $\delta^{13}\text{C}$ and $\delta^{18}\text{O}$ values of $-5.36\text{--}-5.94\text{‰}$ and $20.94\text{--}27.91\text{‰}$, respectively, and these samples fall close to the evolution line of decarboxylation of organic matter in $\delta^{13}\text{C}$ – $\delta^{18}\text{O}$ diagram, also suggesting a genetic relationship between the bleaching and hydrocarbon-bearing fluids. Petrol–mineral composition changes and sulfide characteristics of red, bleached, mineralized zones, as well as pyrite locally replaced by coarse-grained galena in the mineralized zone, imply that the bleaching may occurred before Zn–Pb mineralization. Mass balance calculation and μ -XRF analysis indicate that large amounts of Fe and minor Zn were extracted from red beds with little or no sulfates; however, the red beds with abundant sulfates may be a sink for leached ore metals during the bleaching process. We therefore propose that the former accumulations of iron sulfides and reduced sulfur in the bleached zones may provide an ideal chemical trap for later Zn–Pb mineralization, and the bleached zones with high ΣS contents are the favorable prospective targets of the Uragen-style sandstone-hosted Zn–Pb deposits.

Keywords: bleaching; red bed; hydrocarbon-bearing fluids; H₂S; Uragen Zn–Pb deposit



Citation: Gao, R.; Xue, C.; Dai, J.; Man, R. Origin of the Bleaching in Lower Cretaceous Continental Red Beds in the Uragen Zn–Pb Deposit, Xinjiang, NW China, and Its Implications for Zn–Pb Mineralization. *Minerals* **2022**, *12*, 740. <https://doi.org/10.3390/min12060740>

Academic Editor: Maria Boni

Received: 6 May 2022

Accepted: 7 June 2022

Published: 10 June 2022

Publisher's Note: MDPI stays neutral with regard to jurisdictional claims in published maps and institutional affiliations.



Copyright: © 2022 by the authors. Licensee MDPI, Basel, Switzerland. This article is an open access article distributed under the terms and conditions of the Creative Commons Attribution (CC BY) license (<https://creativecommons.org/licenses/by/4.0/>).

1. Introduction

Continental red bed basins contain abundant oil and gas resources and sandstone-hosted Cu, Pb–Zn, U deposits [1–5], and bleaching of continental red beds is closely related to hydrocarbon micro-seepages and its migration [6,7], as well as to the formation of these sandstone-hosted ore deposits and location of their orebodies [8–13]. The bleaching therefore has become an important prospective indicator [11–13]. However, there are still some uncertain questions regarding the role of the bleaching in sandstone-hosted metallic mineralization, having been classified as either chemical traps including enhancing

porosities and permeabilities [14,15] and providing a reduced environment for later mineralization [8,10,11,15] or leaching of ore metals from the fertile red beds during the bleaching process [13,16].

The Ulugqat basin in the Kashgar thrust-fold belt in front of the South Tianshan Orogen contains many oil–gas fields and sandstone-hosted lead–zinc, copper, uranium ore deposits, including the Uragen giant Zn–Pb deposit, the Kangxi medium-scale Zn–Pb deposit, the Sarek large-scale Cu–Ag deposit and the Bashibulake large-scale U deposit, and it has become an important energy and non-ferrous metal mineral base in northwestern China [3,4,13]. Of these metallic deposits, the Uragen Zn–Pb deposit is the largest one with a proven reserve of 5.90 Mt metals in the southern ore zone and potentially 10 Mt metals for the whole deposit [17,18]. The large-scale Zn–Pb mineralization is strictly confined in the bleached sandstone and conglomerate within the fifth member of the Lower Cretaceous Kezilesu Group, which is probably the fertile source beds of ore metals indicated by the similar Pb isotopic compositions and uniform chondrite-normalized REE distribution patterns with ore sulfides [13,19,20]. Substantial amounts of leachable Fe–Zn–Pb may have been extracted from the red clastic rocks of the fifth member of the Lower Cretaceous Kezilesu Group in the periphery of the mining area during the bleaching process based on mass balance calculations [13]. The bleaching is therefore used as an important prospective indicator for regional sandstone-hosted Zn–Pb deposits of Uragen style [12,13,18,21]. However, the origin of bleaching and its relationship with Zn–Pb mineralization are still unclear due to a lack of geological and geochemical characteristics studies, although the bleaching is generally attributed to natural oil–gas seepage in the Ulugqat basin [12,13,17,22–24]. A large number of residual red sandstone patches or blocks was recently observed in the bleached clastic rocks of the fifth member of the Lower Cretaceous Kezilesu Group without intense Zn–Pb mineralization, which provides an excellent opportunity to study the origin of the bleaching and its relationship with the sandstone-hosted Zn–Pb mineralization.

In this study, the geological and geochemical characteristics of the bleaching were determined based on detailed field investigation and petrographic observation, TESCAN-integrated mineral analyzer (TIMA), and X-ray fluorescence (μ -XRF) analysis of the red and bleached sandstone at the same sedimentary layer. The mass transfer during the bleaching process was also evaluated through mass balance calculations of whole-rock major and trace elements. Combined with previous studies, these results are aimed to decipher the genetic model of the bleaching and its relationship with the sandstone-hosted Zn–Pb mineralization, as well as its significance for regional mineral exploration of similar types in the thrust-fold belts in front of the South Tianshan Orogen.

2. Geological Setting

2.1. Regional Geology

The Ulugqat basin is a typical Meso-Cenozoic intracontinental subbasin in the westernmost part of the southwestern Tarim basin (Figure 1a) [2,17,25], and its formation and evolution were controlled by the South Tianshan Orogen to the north, the Pamir salient to the south, and the Talas–Fergana strike-slip fault (Figure 1a) [17,25,26]. The basin contains a thick section of Jurassic to Quaternary sedimentary series overlying the Paleozoic sedimentary rocks that rest on a Precambrian metamorphic basement (Figure 1b) [17]. The Jurassic–Quaternary sedimentary sequences in the basin are characterized by a ternary basin structure, forming regional well-developed source–reservoir–cap assemblage [13]. The Lower Cretaceous continental red beds are the regional oil and gas reservoir and ore-bearing rocks of regional sandstone-hosted Zn–Pb, Cu and U deposits [13]. The underlying Middle-upper Jurassic lacustrine coal-bearing successions were regarded as important regional source beds for the Yangye oil showing and the Akmomu oilfield in the basin and its periphery based on detailed petroleum geochemistry [22,23], while the overlying Paleocene thick evaporative and argillaceous dolomite were considered as good sedimentary cap rocks [27,28]. Various mineral deposits and energy resources were proven in the

sedimentary sequences of the basin, including copper (Upper Jurassic, Lower Cretaceous and Miocene), zinc-lead (Lower Cretaceous and Paleocene), uranium (Lower Cretaceous), halite (Paleocene), strontium (Lower Cretaceous), coal (Lower Jurassic), and oil and gas (Lower Cretaceous) [17,21,29].

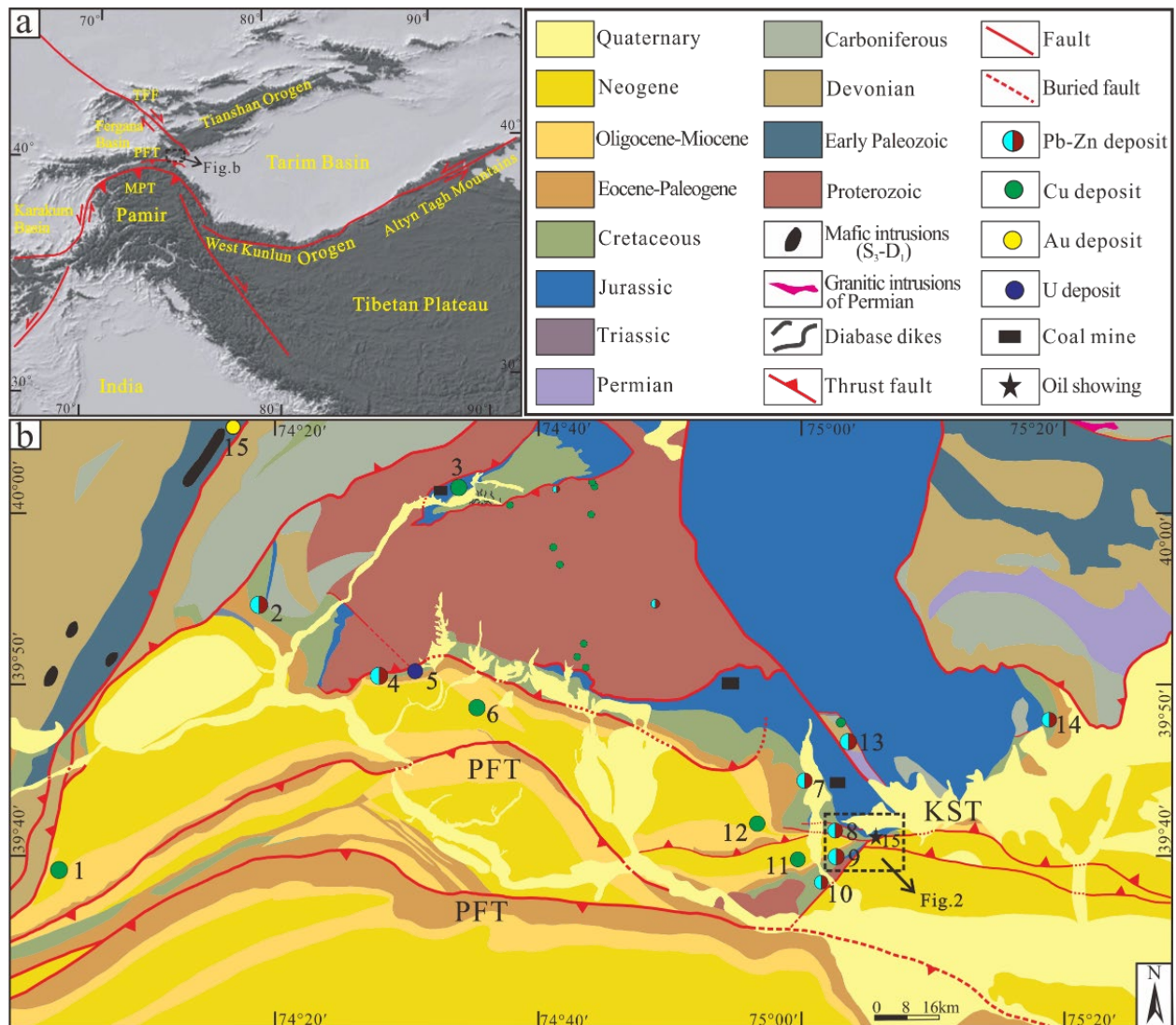


Figure 1. (a) Tectonic framework of central Asia showing the location of the Ulugqat basin in the southwestern Tarim basin and relationships with Tianshan and Western Kunlun orogens (modified after [13,26]). (b) Geological and tectonic sketch map of the Ulugqat foreland basin in front of the South Tianshan Orogen (modified after [2,13]). MPT, Main Pamir Thrust; PFT, Pamir Frontal Thrust; TFF, Talas–Fergana Fault; KST, Kangsu South Thrust; 1, Sahaer Cu deposit; 2, Jiangejieer Zn–Pb deposit; 3, Sareke Cu–Ag deposit; 4, Jiassi Zn–Pb deposit; 5, Bashibulake U deposit; 6, Xiaoruobulake Cu deposit; 7, Kangxi Zn–Pb deposit; 8, northern zone of the Uragen Zn–Pb deposit; 9, southern zone of the Uragen Zn–Pb deposit; 10, Jilege Zn–Pb deposit; 11, Huayuan Cu deposit; 12, Wudong Cu deposit; 13, Shalitashi Zn–Pb deposit; 14, Heiziwei Zn–Pb deposit; 15, Sawayaerdun Au deposit.

2.2. Geology of the Uragen Zn–Pb Deposit

The Uragen Zn–Pb deposit is located in the eastern segment of the Ulugqat basin (Figure 1b). The strata outcropping comprises the Proterozoic Akesu Group and sedimentary sequences from the Lower Jurassic to the Quaternary in ascending order (Figures 2 and 3) [13,17]. The Lower Cretaceous Kezilesu Group is composed of alluvial and braided fluvial red bed sediments that were deposited in a warm arid to semi-arid climate, which

is the sedimentary response to the collision between Lhasa and Qiangtang blocks [30]. The Kezilesu group is divided into five members from bottom to top [17,31], and the fifth member (ore-bearing horizon) is characterized by conglomerate, pebbly sandstone, gravelly sandstone, and sandstone with intercalated mudstone [13]. These coarse-grained clastic rocks were probably derived from the Proterozoic metamorphic basement and the Paleozoic sedimentary rocks with high Zn–Pb contents in the South Tianshan Orogen based on a comprehensive provenance study on sedimentology, petrology and detrital zircon U–Pb geochronology [30], and they formed the most important fertile source beds for the Uragen sandstone-hosted Zn–Pb deposit.

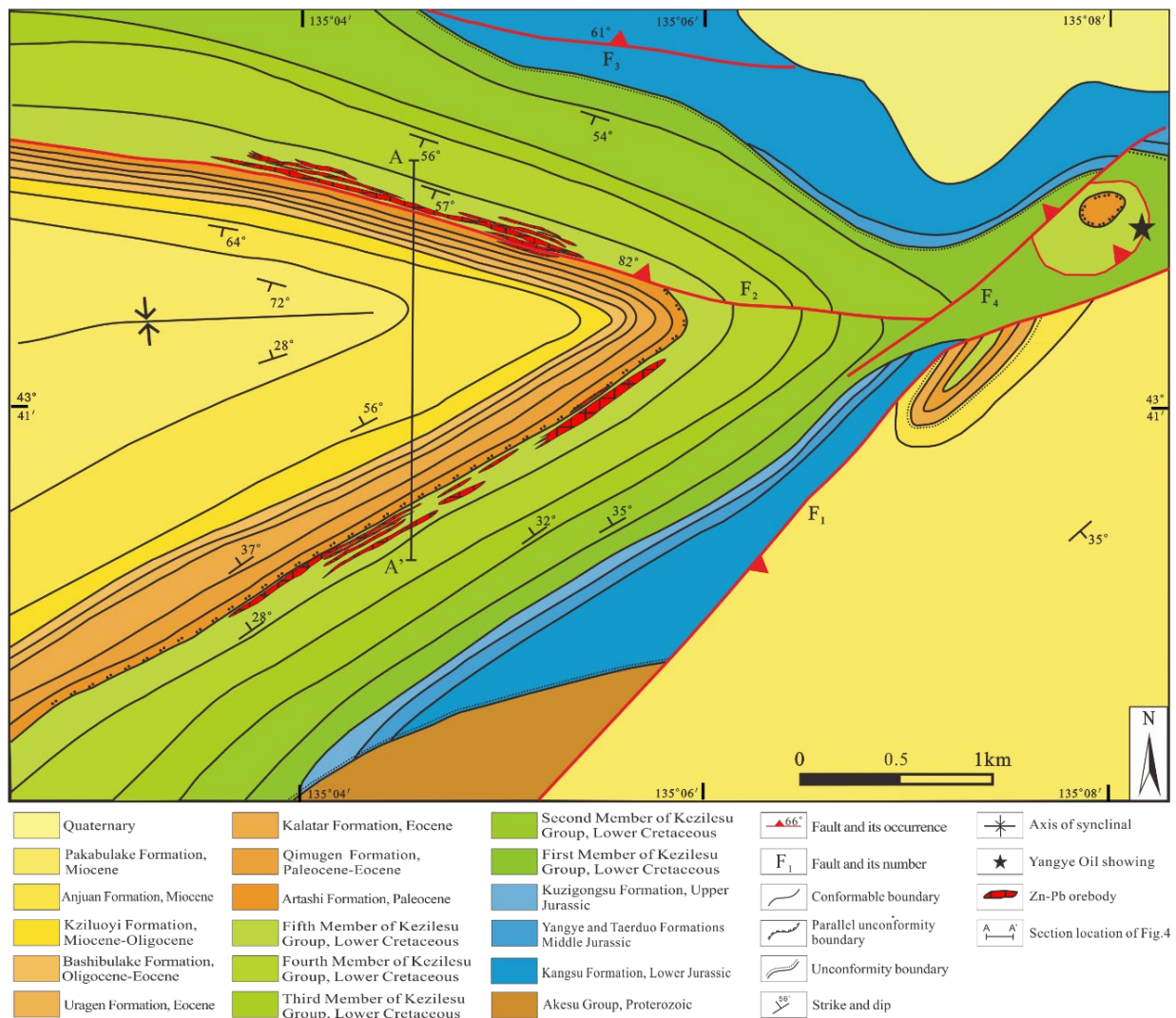


Figure 2. Geological map of the Uragen Zn–Pb deposit and surrounding area (modified after [17,24]). The location of profile A–A' has been outlined.

The deposit is divided into northern and southern ore zones by the axis of the east/west-trending Uragen syncline (Figures 2 and 3). The northern ore zone has an average thickness of ~100 m, a trending length of more than 3.5 km and grades of 0.03–0.47% Pb and 2.24–3.41% Zn [17]. The southern ore zone has an average thickness of ~150 m, a trending length of more than 4.0 km and grades of 0.23–0.89% Pb and 1.69–3.64% Zn [17]. The orebodies are stratiform, tabular and developed on both limbs of the Uragen syncline (Figure 2), as well as in the hinge area at depth (Figure 3), where Zn–Pb mineralization was detected by the deepest drill holes, indicating that the two ore zones are connected spatially (Figure 3) [13,17].

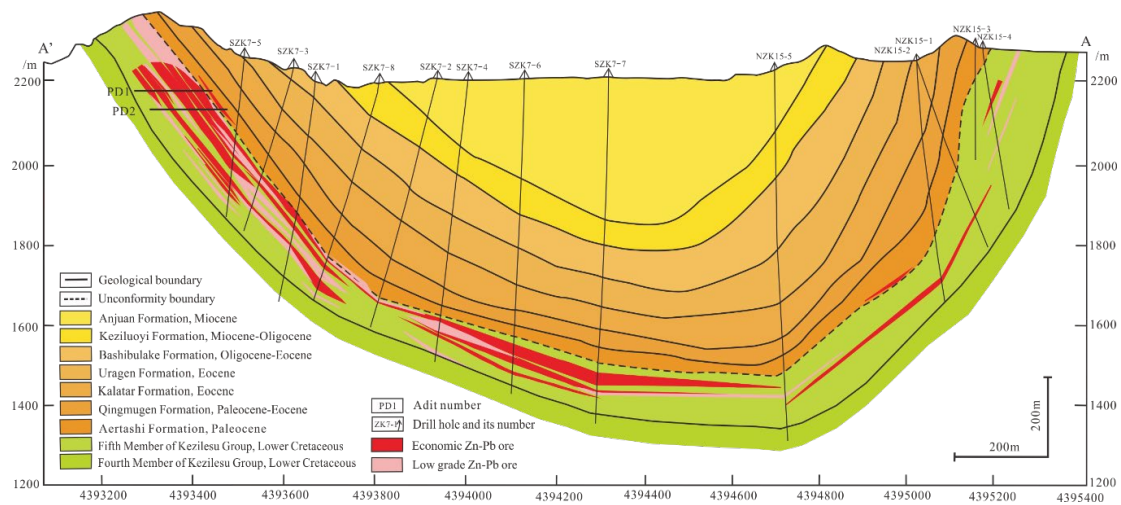


Figure 3. Profile A–A’ of the Uragen Zn–Pb deposit and the location is shown in Figure 2 (modified after [17]).

The orebodies are mainly hosted in the bleached coarse-grained sandstone and conglomerate of the fifth member of the Lower Cretaceous Kezilesu Group due to the reduction by oil–gas infillings [13,17,22–24] and hosted to a lesser extent in the slump breccia of the grey argillaceous dolomite of the Paleocene Aertashi Formation because of dissolution of the lower massive gypsum (Figures 3 and 4) [13,24]. Overall, the orebodies are strictly confined to the bleached zones within the fifth member of the Lower Cretaceous Kezilesu Group, indicating that mineralization in the Uragen deposit has a close spatial relationship with the bleaching [13]. The Zn–Pb mineralization occurs mainly as disseminated sulfides in the matrix and cements of sandstones and conglomerates, and locally as massive sulfides, patches and veinlets of sulfides in some open spaces of the sandstone, conglomerate or dolomite breccia [13,17,32]. Petrographic observations have revealed that iron sulfides formed before Zn–Pb mineralization, indicated by pyrite and marcasite replaced and/or enclosed by sphalerite and galena [13,17]. The overall paragenetic sequence is summarized in Figure 4.

Paragenetic sequence Processes & Minerals	Pre-ore stage		Ore stage	Post-ore stage
	Diagenesis	Oil-gas infilling	Hydrothermal mineralization	Supergene
Reddening	[Red bar]			
Iron hydroxide	[Red bar]			
Hematite	[Red bar]			
Bleaching		[Red bar]		
Calcite	[Red bar]		[Red bar]	
Dolomite	[Red bar]		[Red bar]	
Gypsum	[Red bar]			[Red bar]
Pyrite			[Red bar]	
Marcasite			[Red bar]	
Sphalerite			[Red bar]	
Galena			[Red bar]	
Limonite				[Red bar]
Simthsonite				[Red bar]
Cerussite				[Red bar]
Jarosite				[Red bar]

Figure 4. Paragenetic sequence of ore and gangue minerals from the Uragen Zn–Pb deposit (modified after [13]).

2.3. Bleaching of the Lower Cretaceous Red Beds

Bleaching of the Lower Cretaceous Kezilesu Group in the Uragen Zn–Pb deposit is generally attributed to natural oil–gas seepage based on the spatial relationship of organic matter and the bleaching [12,13,17,22,23], including organic matter on the interface between the bleached and red sandstone [13], oil fillings or stains, and solid bitumen in the pore spaces and fractures [17,22], and hydrocarbon-bearing fluid inclusions in sphalerite, detrital quartz and calcite cements of bleached sandstones [23,24]. The bleached zones are prominently distributed in the fifth member (uppermost parts) of the Lower Cretaceous Kezilesu Group (Figure 5a) with residual preserved red mudstone interlayers containing the bleached “veins” (Figure 5b) and irregular or patchy red mudstone (Figure 5c), sandstone (Figure 5d,e) and pebbly sandstone (Figure 5f). Field investigation reveals that the bleaching crosscut sedimentary bedding (Figure 5d,e) and the bleached “veins” locally crosscut the red beds (Figure 5b), indicating that the bleaching occurred after the sedimentation. The bleaching may result from the dissolution of ferric iron oxide and hydroxide such as hematite pigment during the oil–gas infilling stage based on detailed petrographic observations [13].

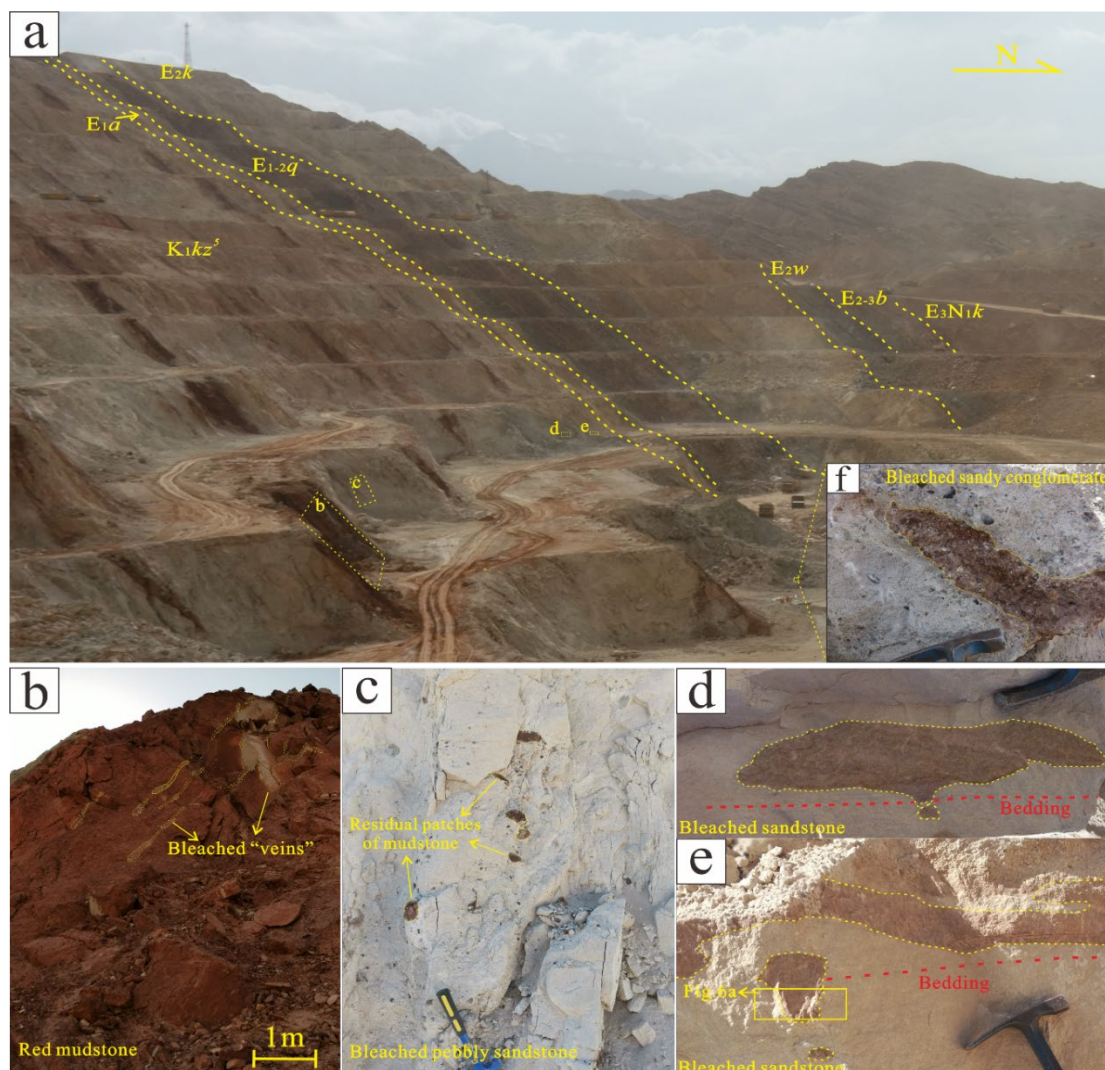


Figure 5. Photographs of the bleaching phenomenon from the fifth member of the Lower Cretaceous Kezilesu Group in the Uragen Zn–Pb deposit. (a) Field photographs of outcropping formations in the west slope of the open pit in the southern ore zone. (b) Red mudstone interbedded crosscut locally by the bleached veins. (c) Residual patches of red mudstone in bleached pebbly sandstone. (d,e) Residual

patches of red sandstones in the bleached sandstone and sedimentary bedding crosscut by the bleached zones. (f) Residual patches of red sandy conglomerate in the bleached sandy conglomerate. The location of sample WG-18 in Figure 6a has been outlined. Lithostratigraphic abbreviations: K₁kz⁵, fifth member of Kezilesu Group, Lower Cretaceous; E₁a, Aertashi Formation, Paleocene; E₁₋₂q, Qimugen Formation, Paleocene–Eocene; E₂k, Kalataer Formation, Eocene; E₂w, Uragen Formation, Eocene; E₂₋₃b, Bashibulake Formation, Oligocene–Eocene; E₃N₁k, Keziluoyi Formation, Miocene–Oligocene.

3. Samples and Analytical Methods

Thirty-two red and bleached sandstone samples were collected from the south ore zone in the Uragen Zn–Pb deposit and were made into polished thin sections for detailed petrographic observations. Zeiss Axioscan 7 fully automatic petrographic analysis microscope was also employed for fluorescence observation using X-Cite Xylis LT720L fluorescence light source, wavelength of 455 nm and intensity of 15%. Of all these samples, WG-18 sample from the slightly mineralized zone at 2104 m level in the west slope of the open pit were selected (Figure 5e), and the red and bleached sandstone at the same sedimentary layer (Figure 6a) was then prepared for petrography, TIMA and μ -XRF studies. Eight powder samples were also obtained from the WG-18 sample using the micro-drilling technology for whole-rock geochemistry analysis and mass balance calculation (Figure 6a). In addition, five calcite samples were collected from calcite cements in bleached sandstone for C–O isotope analysis.

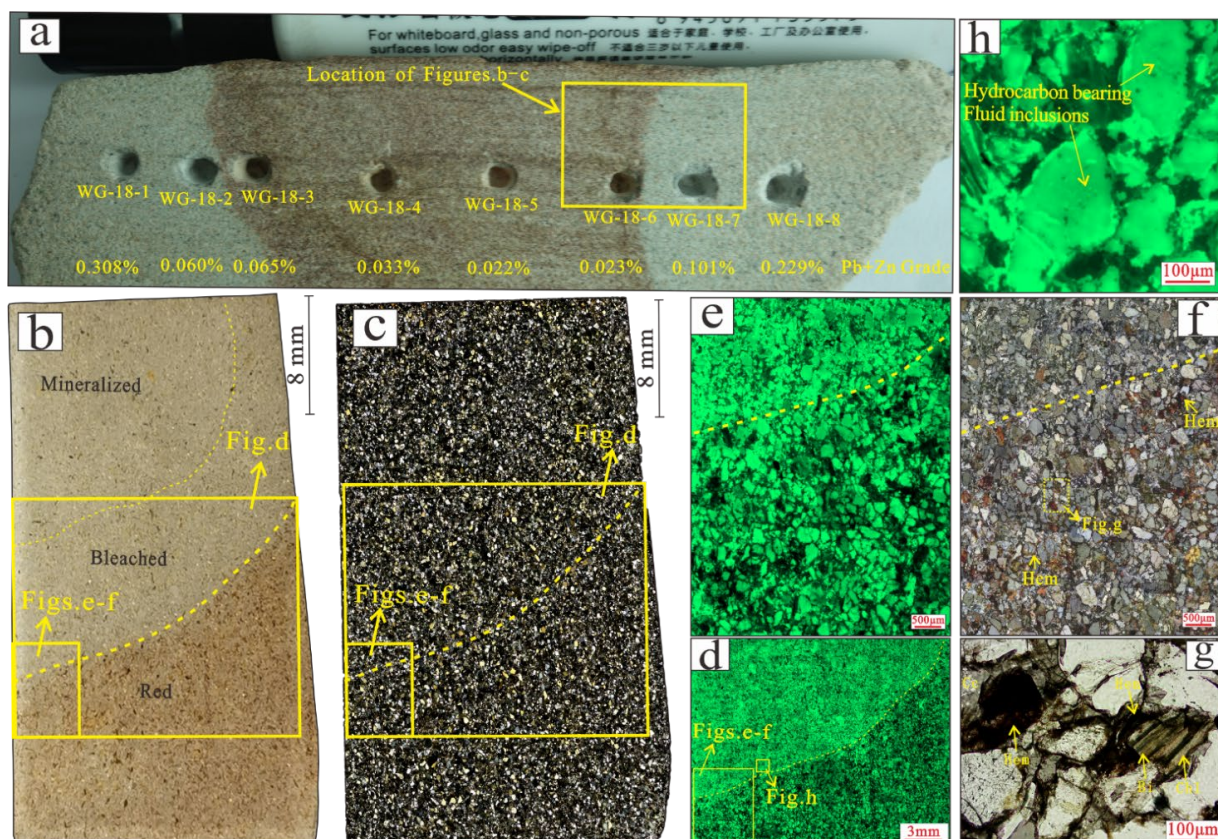


Figure 6. Photographs and photomicrographs of red and bleached sandstone at the same sedimentary layer from the fifth member of the Lower Cretaceous Kezilesu Group in the Uragen Zn–Pb deposit. (a) Photograph of WG-18 sample with the micro-drilling holes showing locations of whole-rock geochemical analysis. (b) Photograph of WG-18 thin section. (c) Panorama of WG-18 thin section under cross-polarized light. (d,e) Fluorescence of the interface between red and bleached sandstone under UV

light. (f,g) Dissolution of IOH and hematite pigment in the bleached sandstone and occurrence of fine-grained hematite in red sandstone under plane-polarized light. (h) Hydrocarbon-bearing fluid inclusions in detrital quartz grains of bleached sandstone showing fluorescence under UV light. Mineral abbreviations: Cc, calcite; Bi, biotite; Chl, chlorite; IOH, ferric iron oxide and hydroxide; Hem, hematite.

3.1. Micro-Area X-ray Fluorescence Surface Scan Analysis (μ -XRF)

The micro-area X-ray fluorescence surface scan analyses were performed by an M4 Plus Micro Area X-ray Fluorescence Analyzer at Guangzhou Tuoyan Analytical Technology Co., Ltd., Guangzhou, China, following previously established procedures [33]. The instrument is equipped with a 20 μ m diameter polycapillary X-ray lens and two X-Flash silicon drift detectors. The scanning was carried out at a 50 kV voltage and a current of 300 μ A, a step of 20 μ m, and an acquisition time of 5 ms for a single pixel in 2 mbar air atmosphere. The M4 tornado software was used to process the original data, analyze the spectral peak information, and derive the element surface distribution map. Semiquantitative data for sixteen elements were evaluated, which included the major elements of Si, Ca, K, Al, Fe, Na, Ti, Mg, S, and Mn, and the minor and trace elements of Zn, Sr, Pb, Zr, Rb, and As.

3.2. Tescan Integrated Mineral Analyzer (TIMA)

Compositional maps were obtained on carbon-coated thin sections using a TESCAN-integrated mineral analyzer under liberation analysis mode at Nanjing Hongchuang Geological Exploration Technology Service Co., Ltd., Nanjing, China, following previously established procedures [34]. The TIMA comprises a Mira-3 scanning electron microscope with four energy dispersive X-ray spectroscopy (EDS, EDAX Element 30). The instrument was operated at an acceleration voltage of 25 kV and a probe current of 9 nA with a working distance of 9 mm. Back-scattered electron (BSE) and energy dispersive X-ray spectroscopy (EDS) data were collected on a regular grid with 6 μ m point spacing. Individual particles and boundaries between different phases were determined based on the BSE image. Mineral identification and mapping are based on the matching between mineral definition files and EDS data. The volume proportion of all phases was automatically calculated.

3.3. Whole-Rock Geochemistry Analysis

Eight powder samples for the whole-rock major and trace elements analyses were obtained from the same sedimentary layer (Figure 6a) and were then crushed and ground to 200 mesh in an agate mill. Whole-rock major and trace elements were performed at Nanjing Hongchuang Geological Exploration Technology Service Co., Ltd. Major element concentrations were determined by a Rigaku-3080 X-ray fluorescence (XRF) employing a Rh-anode X-ray tube with a voltage of 40 kV and a current of 70 mA after samples were fused in a high-frequency melting furnace. The analytical precision (relative standard deviation) and accuracy (relative error) are both better than 2% for the major element concentrations determined during this study. Trace element compositions were determined by an Agilent 7700e inductively coupled plasma-mass spectrometer (ICP-MS), according to the National Standard of China (GB/T14506.30-2010). The analytical accuracy is better than 5% for most elements.

3.4. Mass Balance Calculation

The isocon method proposed by Grant (1986) was used to estimate which elements were lost and which were gained during the bleaching process [35]. The equations that are used to describe the relationship of the concentrations of major and trace elements between red and bleached sandstones are as follows:

$$M_k^B = M_k^R + \Delta M_k^{R-B} \quad (1)$$

$$C_k^B \times M^B/M^R = M_k^B/M^R = M_k^R/M^R + \Delta M_k^{R-B}/M^R = C_k^R + \Delta C_k^{R-B} \quad (2)$$

where C_k^R and C_k^B represent the concentration of element k before and after bleaching, respectively, and M^R and M^B represent the total mass of the rocks before and after bleaching, respectively. ΔM_k^{R-B} and ΔC_k^{R-B} represent the mass and concentration changes of element k during the bleaching process. Equation (2) can be further rewritten as:

$$C_k^B = M^R/M^B \times (C_k^R + \Delta C_k^{R-B}) \quad (3)$$

If the element i is immobile during the bleaching process, the ΔC_i^{R-B} value is zero. Equation (3) can be simplified as:

$$C_i^B = (M^R/M^B) \times C_i^R \quad (4)$$

Equation (4) can be expressed as a line through the original point with the slope of M^R/M^B in the C^R - C^B diagram, and this line is called the isocon.

If the element m is mobile during the bleaching process, the ΔC_m^{R-B} value is not zero. Equation (3) can be expressed as:

$$C_m^B = M^R/M^B \times (1 + \Delta C_m^{R-B}/C_m^R) \times C_m^R \quad (5)$$

Equation (5) can be also expressed as a line through the original point with the slope of $M^R/M^B \times (1 + \Delta C_m^{R-B}/C_m^R)$ in the C^R - C^B diagram. If the slope is larger than the isocon, ΔC_m^{R-B} and ΔM_m^{R-B} are both larger than zero.

According to this principle, the measured concentration of any component for major and trace elements is a plot on the C^R - C^B diagram to obtain a series of points. If the point is below the isocon, the element is lost. Conversely, if the point is above the isocon, the element is gained. The degree of element gain and loss can also be judged based on the deviation of the points from the isocon. In addition, the concentration of any component can be scaled at the same time, according to the requirement details, which does not affect the mass balance analysis results.

3.5. C-O Isotope Analysis

The calcite samples were picked and crushed to 200 mesh-sized powder in preparation. The samples were then digested with 100% phosphoric acid (H_3PO_4) and a MAT-251EM mass spectrometer (Thermo Fisher Scientific, Waltham, MA, USA), at the State Key Laboratory of Geological Processes and Mineral Resource, China University of Geosciences, Beijing, China. The CO_2 gas produced by the reaction of phosphoric acid with the sample at 25 °C was analyzed to yield the C and O isotopic compositions of calcite. Isotopic compositions are reported relative to Pee Dee Belemnite (PDB) for $\delta^{13}C$, and the oxygen isotopic compositions were converted to $\delta^{18}O_{SMOW}$ and expressed as $\delta^{18}O_{SMOW} = 1.03086 \times \delta^{18}O_{PDB} + 30.86$ [36]. The analytical precisions were better than 0.1‰ for carbon isotopes and 0.2‰ for oxygen isotopes.

4. Results

4.1. Petro-Mineral Composition

Detailed petrographic observations (Figure 6) and TIMA mapping results (Figures 7 and 8) indicate that some distinct differences in mineral compositions occurred in the red, bleached and slightly mineralized sandstone at the same sedimentary layer. By comparison, the ferric iron oxide and hydroxide (IOH), such as hematite pigments, was detected in the red sandstones and bleached front zones (Figures 6f–g, 7a and 8), while the sulfides including pyrite, galena and minor sphalerite occurred only in the bleached and slightly mineralized sandstones (Figures 7d,h and 8). The contents of biotite and calcite decreased from red to bleached sandstone zones (Figures 7b,c and 8), whereas the contents of kaolinite, muscovite and ankerite gradually increased from proximal to distal bleaching zones (Figures 7e,g and 8). However, the fine-grained barite grains were only distributed in the bleached zones (Figures 7f and 8) and were locally replaced by fine-grained pyrite

(Figure 7f1). In addition, the detrital grains and calcite cements in the bleached and slightly mineralized zones show bright yellowish green fluorescence, but only some detrital grains and cements in the red sandstone close to the bleached front zone exhibit yellowish green fluorescence (Figure 6d,e), indicating the close spatial relationship between the bleaching and hydrocarbon accumulations and some oil–gas infilling these residual red sandstones. Some hydrocarbon-bearing fluid inclusions have also been detected in detrital quartz grains of bleached sandstone by fluorescence (Figure 6e), which provides direct evidence of hydrocarbon migration within the sandstone interval.

4.2. Elemental Distribution

Elemental mapping using μ -XRF on red and bleached sandstones at the same sedimentary layer suggests that most elements have obvious zoning, indicating the mobilities of ore metals (Figure 9). Fe, Ca, Mg and K contents gradually decrease from red to bleached, to mineralized sandstone zones (Figure 9a,b,f–h), possibly resulting from the dissolution of hematite, biotite, calcite and K-feldspar. The contents of Zn and Mn were also relatively low in the bleached front zones compared to the red sandstone (Figure 9c,e), suggesting the migration of Zn–Mn during the bleaching process. However, the contents of Pb were enriched in the mineralized and bleached distal zones (Figure 9d) due to the presence of galena, and the contents of S were relatively high in the bleached zone compared to the slightly mineralized zone (Figure 9i), which is related to the accumulation of fine-grained pyrite, galena and barite. In addition, Zr is homogeneously distributed in red, bleached and mineralized sandstone zones (Figure 9j), indicating that Zr is stable during the bleaching and mineralization process.

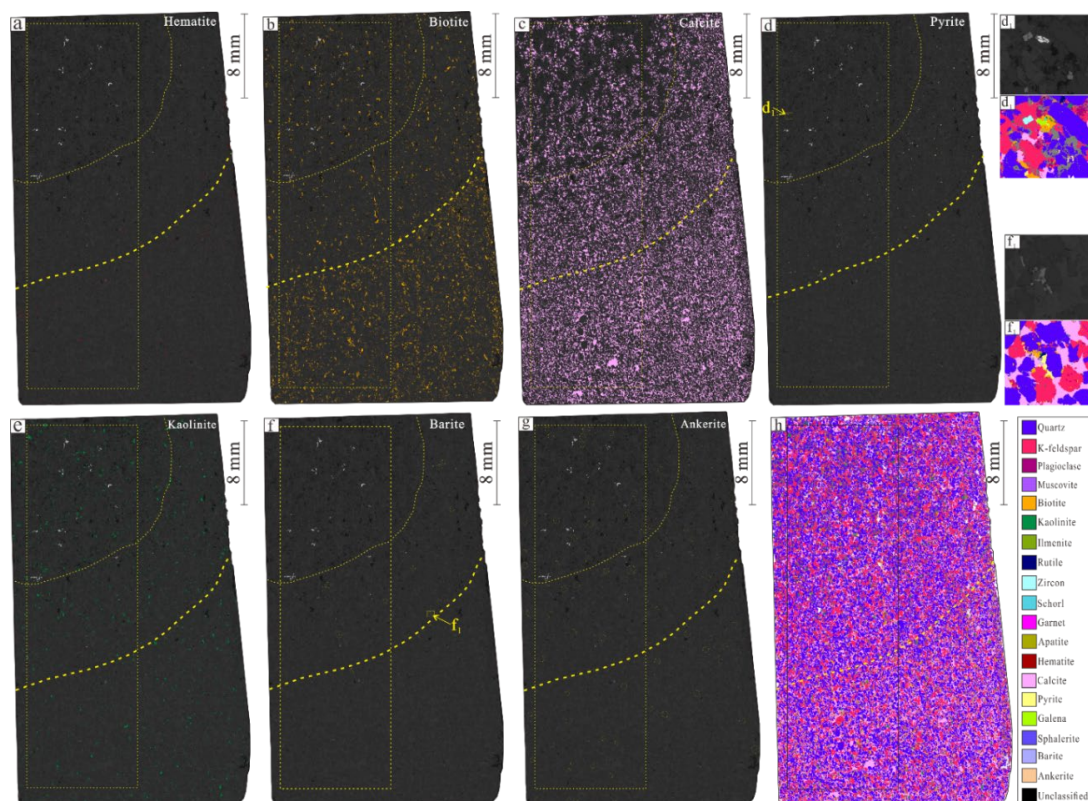


Figure 7. The mineral identification and mapping of red and bleached sandstone at the same sedimentary layer from the fifth member of the Lower Cretaceous Kezilesu Group used by TIMA. The distributions of hematite (a), biotite (b), calcite (c), pyrite (d), kaolinite (e), barite (f), ankerite (g) and whole phases (h) are shown in the red, bleached, and mineralized zones. Barite locally replaced by pyrite in the bleached front zone was shown in (f1), and fine-grained pyrite locally replaced by coarse-grained galena in the leached, slightly mineralized zone was shown in (d1).

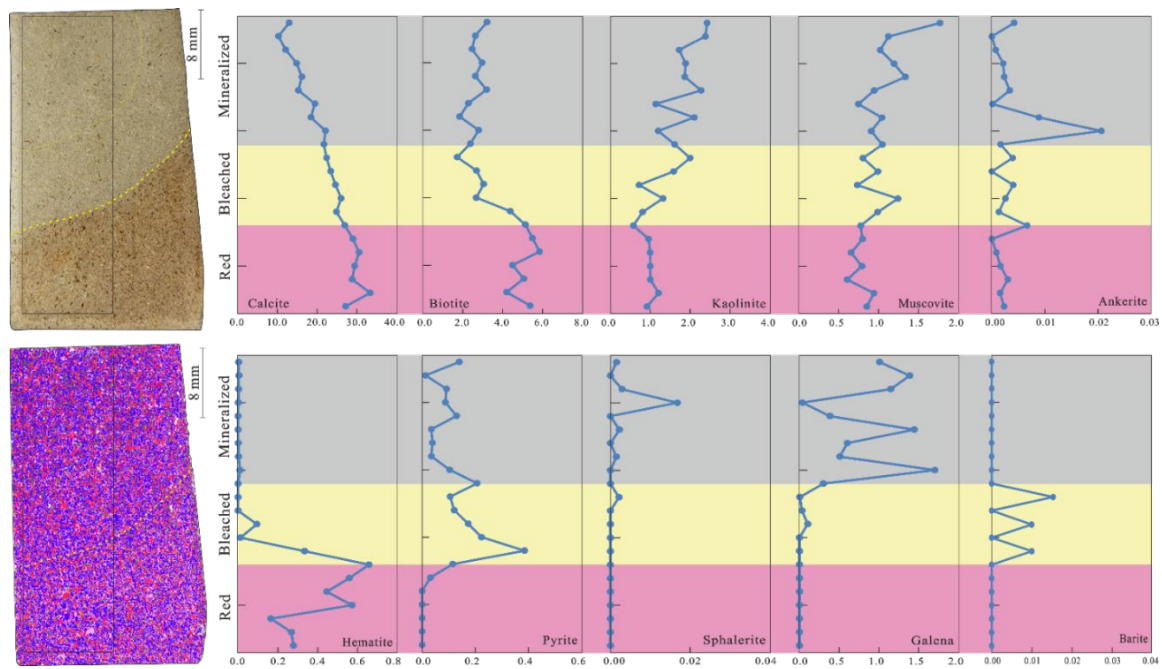


Figure 8. The changes in mineral percentage of red and bleached sandstone in the different zones by TIMA.

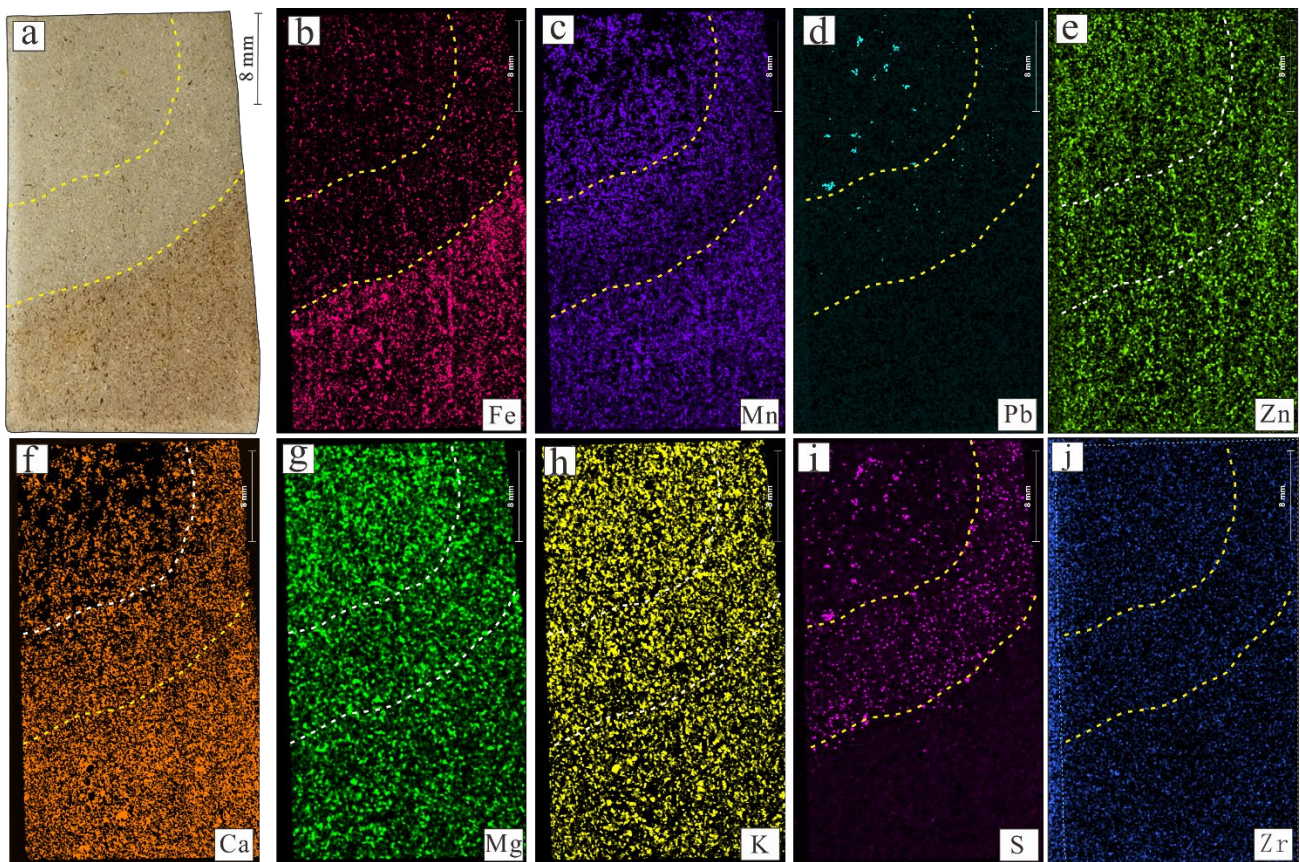


Figure 9. Thin section (a) and corresponding μ -XRF element mapping for Fe (b), Mn (c), Pb (d), Zn (e), Ca (f), Mg (g), K (h), S (i) and Zr (j) of red and bleached sandstone at the same sedimentary layer from the fifth member of the Lower Cretaceous Kezilesu Group, illustrating sample scale chemical characterization.

4.3. Whole-Rock Major and Trace Elements

The major and trace element contents of the red and bleached sandstone samples at the same sedimentary layer are listed in Table 1. These samples all show high LOI contents (10.98–15.10% for red sandstones and 8.20–11.05% for bleached, slightly mineralized sandstones), and relatively low SO₃ contents (0.016–0.120% for red sandstones and 0.391–0.437% for bleached, slightly mineralized sandstones). The good linear correlation between LOI and CaO indicates that calcite accounts for the high LOI contents. Meanwhile, these samples also show linear correlations between Zr and Ti, Th, Hf, Nb, and Yb, suggesting that the bleaching processes had no significant effects on high field-strength elements. We therefore can use Zr as a reference for mobilities of other major and trace elements, as it has been widely used in similar studies regarding bleaching [34,37]. In this paper, using average whole-rock major and trace elemental concentrations of red and bleached, slightly mineralized sandstone at the same sedimentary layer (Table 1), an isocon diagram was constructed to evaluate element gains and losses during the bleaching process (Figure 10). The gained elements mainly include SO₃, MnO, Pb, and Mo, while the lost elements mainly contain FeO_T, CaO, Zn, V, and Sb (Figure 10).

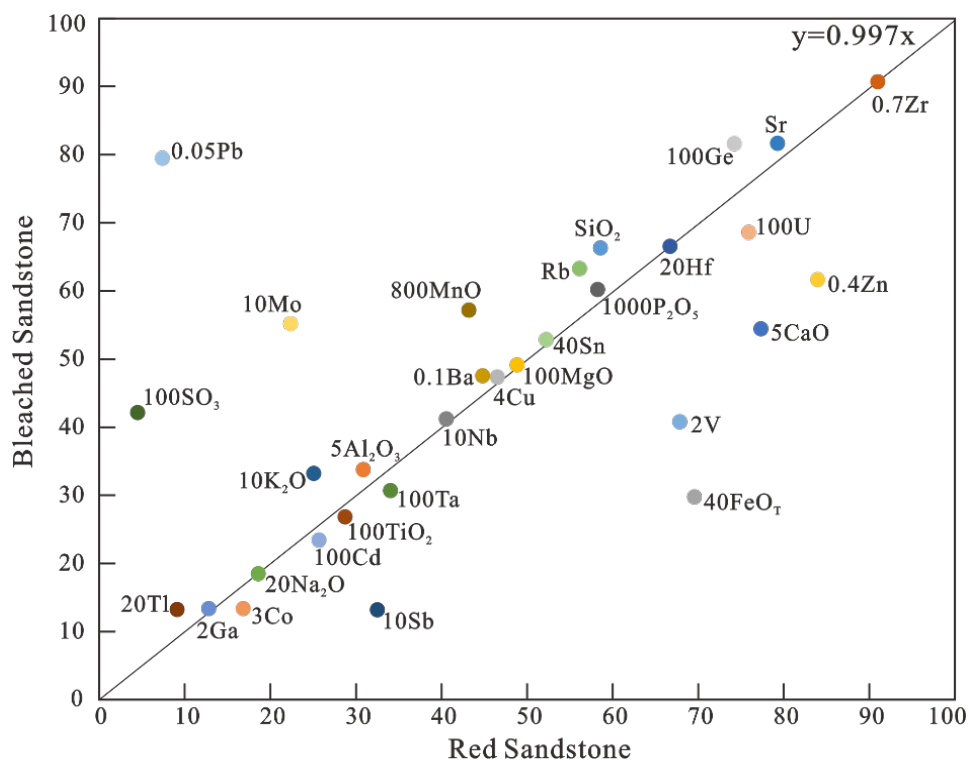


Figure 10. Isocon plots for major (%) and trace elements (ppm) of the red and bleached (slightly mineralized) sandstone at the same sedimentary layer in the fifth member of the Lower Cretaceous Kezilesu Group.

Table 1. Major and trace element contents of red and bleached sandstone at the same sedimentary layer in the Uragen Zn–Pb deposit.

Sample Types		Red Sandstone					Bleached Sandstone (Slightly Mineralized)				
Sample No.		WG18-3	WG18-4	WG18-5	WG18-6	Average	WG18-1	WG18-2	WG18-7	WG18-8	Average
SiO ₂	%	62.71	58.65	55.33	57.65	58.59	68.32	64.82	63.21	68.91	66.32
Al ₂ O ₃	%	6.64	6.35	5.81	5.88	6.17	7.06	6.65	6.34	6.99	6.76
FeO _T	%	2.05	1.65	1.35	1.91	1.74	0.76	0.74	0.76	0.73	0.74
MgO	%	0.52	0.50	0.46	0.48	0.49	0.57	0.45	0.44	0.51	0.49
CaO	%	12.21	15.65	17.77	16.23	15.46	9.22	11.79	13.01	9.54	10.89
Na ₂ O	%	0.91	0.99	0.93	0.89	0.93	1.06	0.87	0.81	0.97	0.93
K ₂ O	%	2.85	2.46	2.26	2.45	2.51	3.37	3.26	3.18	3.49	3.32
TiO ₂	%	0.351	0.308	0.243	0.247	0.287	0.305	0.209	0.267	0.294	0.269
P ₂ O ₅	%	0.068	0.059	0.052	0.054	0.058	0.063	0.058	0.059	0.061	0.060
MnO	%	0.047	0.057	0.058	0.054	0.054	0.081	0.049	0.076	0.080	0.072
LOI	%	10.98	13.62	15.10	14.02	13.43	8.20	10.39	11.05	8.33	9.49
SUM	%	99.34	100.28	99.36	99.87	99.71	99.00	99.28	99.20	99.91	99.35
SO ₃	%	0.120	0.023	0.016	0.020	0.045	0.431	0.428	0.437	0.391	0.422
FeO	%	0.41	0.41	0.27	0.34	0.36	0.36	0.63	0.56	0.29	0.46
Fe ₂ O ₃	%	1.59	1.19	1.05	1.53	1.34	0.36	0.04	0.14	0.40	0.23
Li	ppm	19.4	19.4	17.1	17.1	18.2	21.6	18.0	13.7	14.0	16.8
Be	ppm	1.54	1.29	1.17	1.34	1.33	1.28	1.45	0.95	1.12	1.20
Sc	ppm	5.8	5.6	4.8	4.9	5.3	4.7	6.3	5.3	3.9	5.1
V	ppm	43	32	23	38	34	23	19	20	19	20
Cr	ppm	54	26	25	22	32	23	21	16	15	19
Co	ppm	6.1	5.4	5.7	5.3	5.6	3.9	4.6	5.3	4.0	4.5
Ni	ppm	14.6	12.8	12.2	14.6	13.6	10.9	12.9	11.1	8.5	10.8
Cu	ppm	24.1	8.9	5.3	8.3	11.6	23.2	13.7	4.9	5.6	11.8
Zn	ppm	288	206	164	182	210	212	144	132	130	154
Ga	ppm	7.23	6.44	5.78	6.19	6.41	7.32	6.79	6.40	6.35	6.71
Rb	ppm	63.6	57.2	50.6	53.1	56.1	65.1	67.8	61.5	58.8	63.3
Sr	ppm	75.9	86.3	81.7	73.3	79.3	80.4	82.9	82.8	80.6	81.7
Y	ppm	14.0	12.2	10.9	11.8	12.2	13.9	32.9	14.1	12.4	18.3
Zr	ppm	199	146	73	103	130	129	134	105	150	130
Nb	ppm	4.8	4.1	3.7	3.6	4.1	4.4	4.0	4.1	4.0	4.1
Cs	ppm	4.73	3.81	3.26	3.86	3.91	4.42	4.07	4.07	3.68	4.06
Ba	ppm	540	432	395	426	448	483	474	475	470	476
La	ppm	16.7	15.3	13.8	14.2	15.0	16.2	15.1	14.4	13.1	14.7
Ce	ppm	27.8	20.3	18.5	21.5	22.0	29.4	24.7	25.8	24.6	26.1
Pr	ppm	3.77	2.99	2.85	3.09	3.18	3.52	3.40	3.28	3.08	3.32
Nd	ppm	14.4	12.1	11.0	12.1	12.4	14.0	12.7	12.7	11.6	12.7
Sm	ppm	2.72	2.15	2.13	2.14	2.28	2.88	3.10	2.62	2.47	2.77
Eu	ppm	0.66	0.49	0.51	0.53	0.55	0.66	0.73	0.60	0.54	0.63
Gd	ppm	2.71	2.30	2.01	2.16	2.29	2.81	4.23	2.65	2.33	3.01
Tb	ppm	0.40	0.32	0.28	0.33	0.33	0.39	0.76	0.40	0.35	0.48
Dy	ppm	2.38	1.97	1.79	1.97	2.02	2.34	4.99	2.26	1.92	2.88
Ho	ppm	0.49	0.41	0.36	0.38	0.41	0.47	1.09	0.49	0.43	0.62
Er	ppm	1.43	1.24	1.02	1.14	1.21	1.45	3.18	1.37	1.34	1.83
Tm	ppm	0.19	0.18	0.14	0.16	0.17	0.20	0.44	0.20	0.20	0.26
Yb	ppm	1.38	1.18	1.11	1.14	1.20	1.35	3.06	1.37	1.24	1.76
Lu	ppm	0.21	0.18	0.17	0.17	0.18	0.21	0.39	0.19	0.19	0.25
Hf	ppm	5.1	3.6	2.0	2.7	3.3	3.5	3.2	2.7	3.9	3.3
Ta	ppm	0.37	0.33	0.40	0.27	0.34	0.32	0.29	0.33	0.29	0.31
Pb	ppm	362.5	121.9	57.6	49.2	147.8	2868.0	456.0	877.2	2158.0	1589.8
Th	ppm	6.82	3.75	3.09	3.44	4.28	4.58	3.65	3.82	4.28	4.08
U	ppm	0.96	0.75	0.68	0.65	0.76	0.81	0.63	0.62	0.69	0.69
As	ppm	37.4	6.3	4.0	6.4	13.5	22.3	9.4	11.3	12.0	13.8
Ge	ppm	0.84	0.70	0.73	0.70	0.74	0.94	0.97	0.67	0.69	0.82
Mo	ppm	3.51	1.95	1.60	1.88	2.23	2.52	16.97	1.25	1.36	5.52
Cd	ppm	0.62	0.19	0.12	0.10	0.26	0.61	0.13	0.07	0.13	0.23
In	ppm	0.024	0.015	0.008	0.009	0.014	0.012	0.006	0.010	0.004	0.008
Sn	ppm	1.6	1.4	1.2	1.0	1.3	1.5	1.4	1.2	1.2	1.3
Sb	ppm	8.66	2.18	0.96	1.19	3.25	3.42	0.52	0.58	0.76	1.32
W	ppm	2.1	1.9	0.8	1.0	1.5	1.5	0.8	0.8	1.0	1.0
Tl	ppm	0.67	0.42	0.36	0.37	0.46	0.70	0.64	0.65	0.65	0.66
Bi	ppm	0.69	0.27	0.19	0.09	0.31	0.56	0.11	0.09	0.12	0.22

4.4. C-O Isotopic Compositions

The carbon and oxygen isotopic compositions of calcite samples from the bleached, grey sandstones are listed in Table 2. The $\delta^{13}\text{C}_{\text{V-PDB}}$ and $\delta^{18}\text{O}_{\text{V-SMOW}}$ values ranged from -5.36‰ to -5.94‰ and from $+20.94\text{‰}$ to $+27.91\text{‰}$, respectively. These results are similar to those of the six calcite samples (except one sample possibly affected by diagenetic calcite) from the bleached sandstones with $\delta^{13}\text{C}_{\text{V-PDB}}$ and $\delta^{18}\text{O}_{\text{V-SMOW}}$ values ranging from -5.1‰ to -7.7‰ and from $+20.9\text{‰}$ to $+31.9\text{‰}$, respectively, reported by Zhu et al. (2010) [24]. In the $\delta^{18}\text{O}_{\text{SMOW}}-\delta^{13}\text{C}_{\text{PDB}}$ diagram (Figure 11), these samples lie close to the evolution line of decarboxylation of organic matter, indicating the addition of hydrocarbon-bearing fluids.

Table 2. C-O isotopic compositions of calcite in the bleached pebbly sandstone of the fifth member of the Lower Cretaceous Kezilesu Group in the Uragen deposit.

Sample No.	Location	Lithology	Mineral	$\delta^{13}\text{C}_{\text{V-PDB}}/\text{‰}$	$\delta^{18}\text{O}_{\text{V-SMOW}}/\text{‰}$
CHO-1	Fifth member of the Lower Cretaceous Kezilesu Group in the south ore zone	Bleached pebbly sandstone	Calcite	-5.50	22.16
CHO-2			Calcite	-5.36	20.94
CHO-3			Calcite	-5.75	27.91
CHO-4			Calcite	-5.63	23.62
CHO-5			Calcite	-5.94	22.60

5. Discussion

5.1. Origin of the Bleaching

Bleaching of the Lower Cretaceous continental red beds in the Uragen Zn–Pb deposit is generally attributed to natural oil–gas seepage based on the occurrence of organic matter in the bleached sandstones [12,13,17,22,23]. However, this interpretation lacks direct geological and geochemical evidence. In this study, a field investigation has revealed that the bleached sandstone zones are widely distributed in the uppermost parts of the fifth member of the Lower Cretaceous Kezilesu Group (Figure 5a), probably resulting from the buoyant, updip-migrating hydrocarbon-bearing fluids, ruling out the possibilities of CO_2 -charged dense brine [38,39]. This hypothesis was also verified by the yellowish green fluorescence in the red sandstones close to the bleaching front zones and bleached sandstones and hydrocarbon-bearing fluid inclusions in the detrital quartz grains of the bleached sandstone showing fluorescence (Figure 6). Moreover, the calcite cements in the bleached sandstones show relatively lower $\delta^{13}\text{C}_{\text{PDB}}$ values than those of the bleached Entrada sandstones related to CO_2 -charged brine [38], and these samples fall close to the evolution line of decarboxylation of organic matter in the $\delta^{18}\text{O}_{\text{SMOW}}-\delta^{13}\text{C}_{\text{PDB}}$ diagram, similar to those from hydrocarbon-related bleaching (Figure 11), such as the Yanan sandstone in Ordos basin, NW China [40–42], the Jingxing sandstone in Lanping-Simao basin, SW China [43–45], and the Wingate and Navajo sandstones in Paradox basin, USA [6,46,47]. These all indicate a genetic relationship between the bleaching and hydrocarbon accumulations.

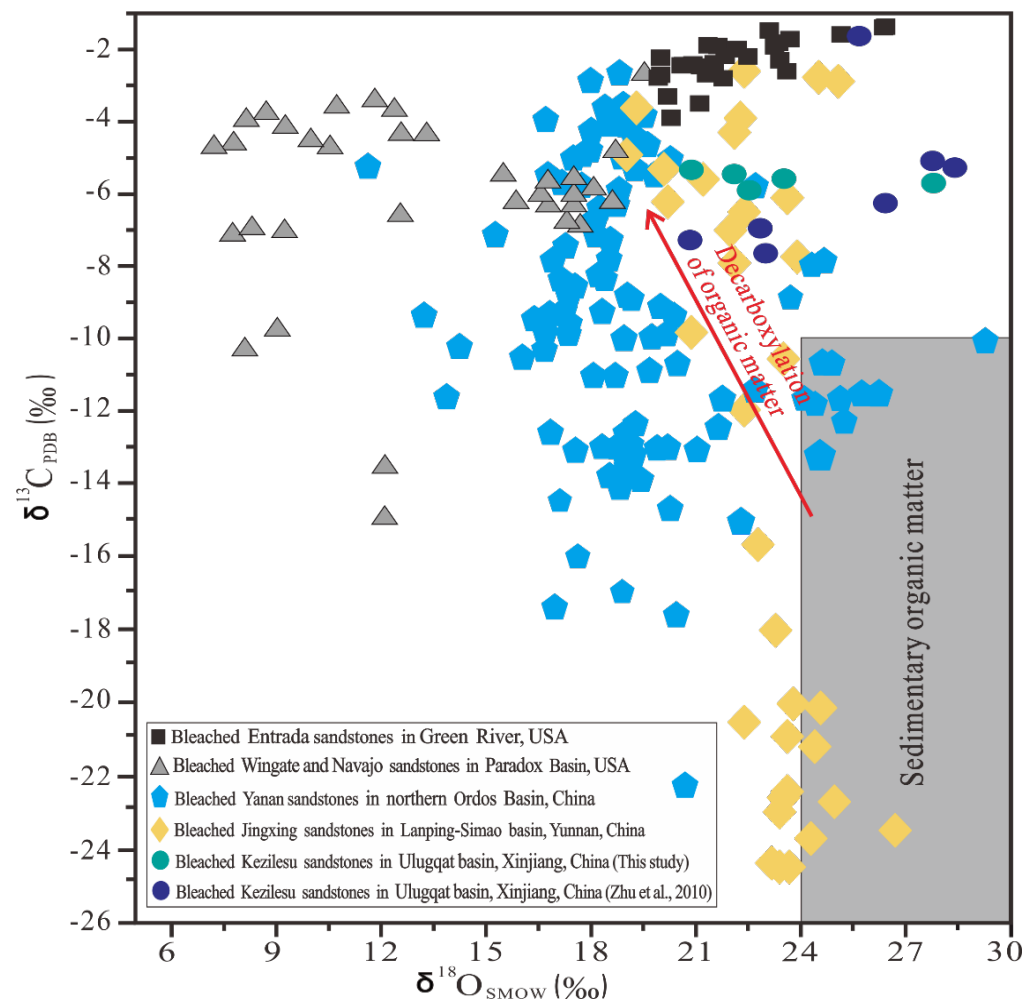


Figure 11. $\delta^{18}\text{O}_{\text{SMOW}}-\delta^{13}\text{C}_{\text{PDB}}$ diagram of calcite in the bleached sandstone from the Uragen deposit and other red beds worldwide, including the Entrada sandstone in Green river, USA [38], the Wingate and Navajo sandstones in Paradox basin, USA [6,46,47], the Yanan sandstone in northern Ordos basin, China [40–42], the Jingxing sandstone in Lanping–Simao basin, China [43–45], and the Kezilesu sandstone in Ulugqat basin, China ([24] and this study).

Petrographic observations have revealed that hematite pigments have close spatial relationship with the bleaching, and the content changes and distributions of plagioclase, biotite, calcite, muscovite, kaolinite and ankerite indicate that the caused fluids resulting in the bleaching are slightly acidic (Figures 6 and 7). The bleaching therefore resulted from the reductive dissolution of hematite pigments during the oil–gas infilling stage, because the Fe^{3+} ions are relatively stable, and they can only migrate on a large scale under the strong acidic environment ($\text{pH} < 4$) [9,46], which cannot be successful to achieve in a natural sandstone reservoir with low compositional maturity. However, the reductive dissolution mechanism of hematite pigments remains uncertain, as hydrocarbon, organic acid and hydrogen sulfide (H_2S) are all possible reducing agents [6,7,9,48]. Previous kinetics studies of hematite dissolution have revealed that the reaction rate of hydrogen sulfide (H_2S) as a reducing agent is significantly faster than that of CH_4 under the same conditions [49,50], and if the reducing fluids contain abundant hydrogen sulfide (H_2S), the hematite will be in situ reduced to form pyrite without a large amount of Fe migration [50]. In the Uragen deposit, the coexistence of pyrite, barite and hematite (Figures 6 and 7), high S contents (Figure 9i) and barite locally replaced by pyrite (Figure 6f1) in the bleached front zone indicate that hydrogen sulfide (H_2S) may play an important role in the bleaching, which was probably formed by in situ sulfate reduction of soluble sulfate in pore water and sulfate

cements. This is consistent with the low S contents in the residual red sandstone patches of the bleached zones (Figure 9i), probably because the pore water with sulfate cannot penetrate them easily due to well-developed diagenetic calcite cement, although some parts in the residual red sandstones possibly show some oil–gas infilling signs, e.g., the fluorescent detrital quartz grains and calcite cements.

5.2. Implications for Zn–Pb Mineralization

Although some geochronological studies have been conducted to date the mineralization of the Uragen Zn–Pb deposit [32] and regional oil–gas infillings [51–53], the temporal relationship between the bleaching and mineralization remains uncertain, largely because the accurate ages of sandstone-hosted Zn–Pb mineralization and oil–gas infilling are notoriously difficult to date [54,55]. The bleaching was regarded as pre-mineralization alteration in this study, as the Zn–Pb mineralization was strictly confined to the bleached zone, and some parts of the bleached zones were not mineralized [24,56]. Detailed petrographic observations have also revealed that the mineralized zone was superimposed on the bleached zone, because the bleached zone is characterized by fine-grained sulfides such as pyrite (Figures 7 and 8) and high S content (Figure 9) while the mineralized zone is represented by coarse-grained galena and fine-grained pyrite (Figures 7 and 8), locally replaced by galena (Figure 7d1). Considering that the bleaching of red beds has been widely used as a prospective indicator for sandstone-hosted Zn–Pb deposits in the South Tianshan, NW China [2,12,13,21], other important ore-controlling factors, except for pre-mineralization bleaching, have to be therefore considered during mineral exploration.

Previous studies have revealed that the Lower Cretaceous Kezilesu Group is probably the fertile source beds of the ore metals based on systemic Pb isotopes [13,19,20] and substantial amounts of leachable Fe–Zn–Pb may have been extracted during the bleaching process [13]. In this study, large amounts of Fe and minor Zn were also extracted from red beds with little or no sulfates, indicated by the low Fe–Mn–Zn contents in the bleached front zone using μ -XRF elemental mapping (Figure 9) and mass balance calculations for major and trace elements of red sandstone and bleached sandstone (slightly Pb mineralized) at the same sedimentary layer (Figure 10). Moreover, hydrocarbon has been considered to play a more active role in the leaching of ore metals from source beds and forming the ore-forming fluid, as ore metals (such as Zn, U, V, Pb, and other elements) can be enriched to high concentrations (some even reaching industrial grades) in liquid hydrocarbon [57–59]. Similarly, reduced sulfur (H_2S) was considered as triggering for the precipitation of metallic sulfides for hydrocarbon-bearing fluids [58,59]. That is, if the red beds bore little or no sulfates, substantial amounts of Fe–Zn could have been extracted. However, if the red beds bore abundant sulfates, the leachable ore metals (especially iron) would have been precipitated from the hydrocarbon-bearing fluids. Consequently, pre-mineralization bleaching of red beds may produce large amounts of iron sulfides and reduced sulfur in local sandstone reservoirs with many sulfate cements and/or sulfate-rich pore water, providing an ideal chemical trap for later sandstone-hosted Zn–Pb mineralization. Therefore, the bleached zones with high ΣS contents are the favorable prospective targets of the Uragen-style sandstone-hosted Zn–Pb deposits.

6. Conclusions

- (1) The bleaching of red beds is related to regional oil–gas infilling, and the dissolution of hematite pigment may result from the interaction with H_2S formed by in situ sulfate reduction in the Uragen Zn–Pb deposit.
- (2) Large amounts of Fe and minor Zn were extracted from red beds with little or no sulfates, and the red beds with considerable sulfate may be a sink for leached ore metals during the bleaching process.
- (3) The bleaching is pre-mineralization alteration, and the former accumulation of iron sulfides and reduced sulfur during the bleaching process may provide chemical traps for later sandstone-hosted Zn–Pb mineralization.

- (4) The bleached zones with high ΣS contents are the favorable prospective targets of the Urogen-style sandstone-hosted Zn–Pb deposits.

Author Contributions: Conceptualization, R.G. and C.X.; investigation, R.G. and R.M.; data curation, R.G.; writing—original draft preparation, R.G.; writing—review and editing, R.G., C.X., J.D. and R.M.; supervision, C.X.; funding acquisition, R.G. and J.D. All authors have read and agreed to the published version of the manuscript.

Funding: This research was jointly supported by the National Natural Science Foundation of China (41902067), the Fundamental Research Funds for the Central Universities (N2124002-10, 2652016072) and the Project funded by the China Postdoctoral Science Foundation (2019M650784) for Rongzhen Gao, and the National Natural Science Foundation of China (42102102) for Junfeng Dai.

Data Availability Statement: Not applicable.

Acknowledgments: The authors would like to thank the managers and geological staff of Xinjiang Zijin Zinc Mining Co., Ltd., China, for their support in our fieldwork. We are also deeply grateful to the anonymous reviewers for their reviews and constructive suggestions.

Conflicts of Interest: The authors declare no conflict of interest.

References

- Liu, C.; Qiu, X.; Wu, B.; Zhao, H. Subdivisions of the Central-east Asia multi-energy minerals metallogenetic domain and types of those basins. *Energy Explor. Exploit.* **2009**, *27*, 153–166. [[CrossRef](#)]
- Fang, W.; Jia, R.; Wang, L. Types of basin fluids, mechanism of discolored alterations and metal mineralizations of glutenite-type Cu–Pb–Zn–U deposits in intercontinental red-bed basin of the western Tarim basin. *J. Earth Sci. Environ.* **2017**, *39*, 585–619. (In Chinese with English Abstract)
- Fang, W.; Wang, L.; Jia, R. Mosaic tectonics of Mesozoic to Cenozoic basin-mountain-plateau in the western Tarim basin: Glutenite-type Cu–Pb–Zn–celesite–U–coal metallogenetic system. *J. Earth Sci. Environ.* **2018**, *40*, 663–705. (In Chinese with English Abstract)
- Fang, W.; Wang, L.; Lu, J.; Li, T.; Jia, R. Mesozoic–Cenozoic sedimentary basin, foreland fold-and-thrust mineralization regularities of copper–lead–zinc–celesite–uranium–cocal in Wulagen, Xinjiang, Chian. *Geotecton. Metallog.* **2020**, *44*, 881–912. (In Chinese with English Abstract)
- Wang, Y.; Yang, L.; Deng, J.; Wu, B.; Li, Z.; Wang, M. Accumulation system of cohabitating multi-energy minerals and their comprehensive exploration in sedimentary basin—a case study of Ordos basin, NW China. *Acta Geol. Sin.* **2014**, *88*, 815–824. (In Chinese with English Abstract)
- Chan, M.A.; Parry, W.T.; Bowman, J.R. Diagenetic hematite and manganese oxides and fault-related fluid flow in Jurassic sandstones, southeastern Utah. *Am. Assoc. Pet. Geol. Bull.* **2000**, *84*, 1281–1310.
- Beitler, B.; Chan, M.A.; Parry, W.T. Bleaching of Jurassic Navajo Sandstone on Colorado Plateau Laramide highs: Evidence of exhumed hydrocarbon supergiants? *Geology* **2003**, *31*, 1041–1044. [[CrossRef](#)]
- Box, S.E.; Syusyura, B.; Seltmann, R.; Creaser, R.A.; Dolgoplova, A.; Zientek, M.L.; Hedenquist, J.W.; Harris, M.; Camus, F. Dzhezkazgan and associated sandstone copper deposits of the Chu–Sarysu Basin, Central Kazakhstan. *Spec. Publ. Soc. Econ. Geol.* **2012**, *16*, 303–328.
- Ma, Y.; Liu, C.; Zhao, J.; Huang, L.; Yu, L.; Wang, J. Characteristics of bleaching of sandstone in northeast of Ordos Basin and its relationship with natural gas leakage. *Sci. China Ser. D Earth Sci.* **2007**, *50* (Suppl. S2), 153–164. [[CrossRef](#)]
- Zhang, L.; Liu, C.; Lei, K. Green altered sandstone related to hydrocarbon migration from the uranium deposits in the northern Ordos Basin, China. *Ore Geol. Rev.* **2019**, *109*, 482–493. [[CrossRef](#)]
- Song, Y.; Hou, Z.; Xue, C.; Huang, S. New Mapping of the World-Class Jinding Zn–Pb Deposit, Lanping Basin, Southwest China: Genesis of Ore Host Rocks and Records of Hydrocarbon–Rock Interaction. *Econ. Geol.* **2020**, *115*, 981–1002. [[CrossRef](#)]
- Wang, L.; Ye, L.; Liu, Z. The “bleaching of sandstone” characteristics and its implications of the Kangxi lead–zinc deposit in Wuqia county, Xinjiang. *Northwestern Geol.* **2016**, *49*, 91–98. (In Chinese with English Abstract)
- Gao, R.; Xue, C.; Zhao, X.; Chen, X.; Li, Z.; Symons, D. Source and possible leaching process of ore metals in the Urogen sandstone-hosted Zn–Pb deposit, Xinjiang, China: Constraints from lead isotopes and rare earth elements geochemistry. *Ore Geol. Rev.* **2019**, *106*, 56–78. [[CrossRef](#)]
- Surdam, R.C.; Jiao, Z.S.; Macgowan, D.B. Redox reactions involving hydrocarbons and mineral oxidants: A mechanism for significant porosity enhancement in sandstones. *Am. Assoc. Pet. Geol. Bull.* **1993**, *83*, 1509–1518.
- Rainoldi, A.L.; Franchini, M.; Pons, G.; Giusiano, A.; Cesaretti, N. The Role of Hydrocarbons in the Genesis of the Sediment-Hosted Stratiform Copper Deposits, Neuquén Basin (Argentina). In Proceedings of the 13th SGA Biennial Meeting, Nancy, France, 24–27 August 2015; pp. 1989–1992.
- Parnell, J.; Wang, X.; Raab, A.; Feldmann, J.; Brolly, C.; Michie, R.; Armstrong, J. Metal flux from dissolution of iron oxide grain coatings in sandstones. *Geofluids* **2021**, *2021*, 5513490. [[CrossRef](#)]

17. Xue, C.; Chi, G.; Li, Z.; Dong, X. Geology, geochemistry and genesis of the Cretaceous and Paleocene sandstone- and conglomerate-hosted Uranium Zn-Pb deposit, Xinjiang, China: A review. *Ore Geol. Rev.* **2014**, *63*, 328–342. [[CrossRef](#)]
18. Yang, B. Red bed Cu-Pb-Zn deposits and mineralization of hot brine in continental red bed basin. *Geol. China* **2018**, *45*, 441–455. (In Chinese with English Abstract)
19. Gao, Y.; Zhang, Z.; Dong, F.; Wang, Z. Trace element geochemistry and S-Pb isotope compositions of the Wulagen Pb-Zn deposit, Xinjiang Province, China. *Acta Geol. Sin. Engl. Ed.* **2014**, *88* (Suppl. S2), 154–155. [[CrossRef](#)]
20. Li, P.; Hu, Y.; Dong, C.; Ren, T.; Guan, S. Characteristics of lead isotopic compositions of sulfides from the Uranium Pb-Zn deposit in Xinjiang, China. *Bull. Mineral. Petrol. Geochem.* **2020**, *39*, 1325–1340. (In Chinese with English Abstract)
21. Liu, Z.; Chen, Z.; Han, F.; Chen, B.; Zhou, Y.; Cui, L.; Jiang, R.; Li, L. Preliminary analysis on the relationship between oil and gas reduction signs and mineralization in the Wulagen lead-zinc deposit in Kashi, Xinjiang. *Miner. Depos.* **2010**, *29* (Suppl. S1), 1049–1050. (In Chinese)
22. Dong, X.; Xue, C.; Li, Z.; Liu, Z. Characteristics and geological significances of the organic matter in the Wulagen Zn-Pb deposit, Kashi sag, Xinjiang. *Earth Sci. Front.* **2013**, *20*, 129–145. (In Chinese with English Abstract)
23. Han, F.; Chen, Z.; Liu, Z.; Chen, B.; Cui, L.; Ding, W.; Jiang, R.; Li, L. Organic geochemistry of Wulagen Pb-Zn deposit in southwest Tianshan mountains and its implications. *Miner. Depos.* **2013**, *32*, 591–602. (In Chinese with English Abstract)
24. Zhu, X.; Wang, J.; Liu, Z.; Fang, T. Geologic characteristics and the genesis of the Wulagen lead-zinc deposit, Xinjiang, China. *Acta Geol. Sin.* **2010**, *84*, 694–702. (In Chinese with English Abstract)
25. Zhou, X.; Luo, J.; Mai, G. *Structural Characteristics and Oil and Gas Geology in the Kashi Sag and Surrounding Areas in the Tarim Basin*; Petroleum Industry Publishing House: Beijing, China, 2005; pp. 1–233. (In Chinese with English Abstract)
26. Sobel, E.R.; Chen, J.; Schoenbohm, L.M.; Thiede, R.; Stockli, D.F.; Sudo, M.; Strecker, M.R. Oceanic-style subduction controls late Cenozoic deformation of the Northern Pamir orogen. *Earth Planet. Sci. Lett.* **2013**, *363*, 204–218. [[CrossRef](#)]
27. Zhao, M.; Xia, X.; Qin, S.; Song, Y.; Liu, S. Gas source study of Ake well 1 resource in Tarim basin. *Nat. Gas Ind.* **2003**, *2*, 31–33. (In Chinese with English Abstract)
28. Hu, J.; Cui, J. Geochemical analysis of crude oils and oil sand in the Kashi Sag, Tarim basin. *Sci. Technol. Eng.* **2015**, *15*, 122–129. (In Chinese with English Abstract)
29. Li, Z.; Xue, C.; Dong, X.; Liu, Z.; Zhong, T.; Qi, S. Ore geology, S- and Pb- isotopic compositions of the Wulagen Zn-Pb deposit, Wuqia county, Xinjiang. *Earth Sci. Front.* **2013**, *20*, 40–54. (In Chinese with English Abstract)
30. Gao, R.; Xue, C.; Chi, G.; Zhao, X.; Man, R.; Ren, D. Provenance of the uppermost clastic rocks of the Lower Cretaceous Kezilesu Group from the Ulugat Basin, Xinjiang, NW China and its tectonic implications: Insights from sedimentary records and detrital zircon U-Pb geochronology. *Geol. J.* **2020**, *55*, 2080–2109. [[CrossRef](#)]
31. Liu, Z.; Tian, P.; Zhu, X.; Chen, Z.; Chen, B.; Qi, S.; Ye, L.; Yu, Z.; Ren, J. Ore-forming geological characteristics and metallogenic model on Wulagen lead-zinc deposit, Xinjiang. *Miner. Explor.* **2011**, *2*, 669–680. (In Chinese with English Abstract)
32. Wang, Y.; Zhang, Z.; Zhang, S.; Cheng, Z.; Huang, H.; Ye, J.; Zhao, Z.; Ma, Y.; Santosh, M. Palaeogene sediment-hosted Pb-Zn deposits in SE Asia: The Uranium example. *Int. Geol. Rev.* **2017**, *59*, 1–13. [[CrossRef](#)]
33. Ma, W.; Deng, T.; Xu, D.; Chi, G.; Li, Z.; Zhou, Y.; Dong, G.; Wang, Z.; Zou, S.; Qian, Q.; et al. Geological and geochemical characteristics of hydrothermal alteration in the Wangu deposit in the central Jiangnan Orogenic Belt and implications for gold mineralization. *Ore Geol. Rev.* **2021**, *139*, 104479. [[CrossRef](#)]
34. Wang, X.; Chen, L.; Hanyu, T.; Zhong, Y.; Shi, J.; Liu, X.; Kawabata, H.; Zeng, G.; Xie, L. Magnesium isotopic fractionation during basalt differentiation as recorded by evolved magmas. *Earth Planet. Sci. Lett.* **2021**, *565*, 116954. [[CrossRef](#)]
35. Grant, J. The isocon diagram—A simple solution to Gresens' equation for metasomatic alteration. *Econ. Geol.* **1986**, *81*, 1976–1982. [[CrossRef](#)]
36. Friedman, I.; O'Neil, J.R. Compilation of stable isotope fractionation factors of geochemical interest. In *Data of Geochemistry*, 6th ed.; U.S. Government Publishing Office: Washington, DC, USA, 1977; pp. 13–59.
37. Chu, H.; Chi, G.; Bosman, S.; Card, C. Diagenetic and geochemical studies of sandstones from drill core DV10-001 in the Athabasca basin, Canada, and implications for uranium mineralization. *J. Geochem. Explor.* **2015**, *148*, 206–230. [[CrossRef](#)]
38. Wigley, M.; Kampman, N.; Dubacq, B.; Bickle, M. Fluid-mineral reactions and trace metal mobilization in an exhumed natural CO₂ reservoir, Green River, Utah. *Geology* **2012**, *40*, 555–558. [[CrossRef](#)]
39. Wigley, M.; Kampman, N.; Chapman, H.J.; Dubacq, B.; Bickle, M.J. In situ redeposition of trace metals mobilized by CO₂-charged brines. *Geochem. Geophys. Geosystems* **2013**, *14*, 1321–1332. [[CrossRef](#)]
40. Cao, B.F.; Bai, G.P.; Zhang, K.X.; Zhang, L.K.; He, B. A comprehensive review of hydrocarbons and genetic model of the sandstone-hosted Dongsheng uranium deposit, Ordos Basin, China. *Geofluids* **2016**, *16*, 624–650. [[CrossRef](#)]
41. Sun, L. Geological Characteristics and Genesis Analysis of Daying Sandstone-Type Uranium Deposit in Ordos Basin. Master's Thesis, Northwest University, Xi'an, China, 2016; pp. 1–76. (In Chinese with English Abstract)
42. Pang, K. The Characteristics of In-Situ Stable Isotopes and Their Geological Significance about Sandstone Uranium Deposits in Northern Ordos Basin. Master's Thesis, Northwest University, Xi'an, China, 2018; pp. 1–106. (In Chinese with English Abstract)
43. Ma, L. The Researches on the Binary Structure and Geochemical Evidence of Jinding Lead-Zinc Deposit in Yunnan Province. Master's Thesis, China University of Geosciences, Beijing, China, 2016; pp. 1–68. (In Chinese with English Abstract)
44. Zheng, H.; Guo, F.; Zhu, Z.; Jiang, Y. Carbon, oxygen and sulfur isotope geochemistry characteristics of the Jinding lead-zinc deposit in Yunnan and their geological significance. *Resour. Surv. Environ.* **2012**, *33*, 218–224. (In Chinese with English Abstract)

45. Tang, Y.; Bi, X.; He, L.; Wu, L.; Feng, C.; Zou, Z.; Tao, Y.; Hu, R. Geochemical characteristics of trace elements, fluid inclusions and carbon-oxygen isotopes of calcites in the Jinding Zn-Pb deposit, Lanping, China. *Acta Petrol. Sin.* **2011**, *27*, 2635–2645. (In Chinese with English Abstract)
46. Garden, I.R.; Guscott, S.C.; Burley, S.D.; Foxford, K.A.; Walsh, J.J.; Marshall, J. An exhumed palaeo-hydrocarbon migration fairway in a faulted carrier system, Entrada Sandstone of SE Utah, USA. *Geofluids* **2001**, *1*, 195–213. [[CrossRef](#)]
47. Eichhubl, P.; Davatzes, N.C.; Becker, S.P. Structural and diagenetic control of fluid migration and cementation along the Moab fault, Utah. *Am. Assoc. Pet. Geol. Bull.* **2009**, *93*, 653–681. [[CrossRef](#)]
48. Beitler, B.; Parry, W.T.; Chan, M.A. Fingerprints of fluid flow: Chemical diagenetic history of the Jurassic Navajo Sandstone, Southern Utah, USA. *J. Sediment. Res.* **2005**, *75*, 547–561. [[CrossRef](#)]
49. Purser, G.; Rochelle, C.A.; Rushton, J.; Pearce, J.M.; Wagner, D. An experimental and analogue study of iron release from red sandstones. *Energy Procedia* **2014**, *63*, 3268–3274. [[CrossRef](#)]
50. Maskell, A.; Scott, P.M.; Buisman, I.; Bickle, M. A siltstone reaction front related to CO₂- and sulfur-bearing fluids: Integrating quantitative elemental mapping with reactive transport modeling. *Am. Mineral.* **2018**, *103*, 314–323. [[CrossRef](#)]
51. Zhang, Y.; Horst, Z.; Andrew, T.; Liu, K.; Luo, X. K-Ar dating of authigenic illite and its applications to study of oil-gas histories of typical sandstone reservoirs, Tarim basin, Northwest China. *Earth Sci. Front.* **2004**, *11*, 637–648. (In Chinese with English Abstract)
52. Zhang, J.; Wang, D.; Wang, Z.; Li, X.; Su, X. Natural gas deposit formation geochemistry of Akmomu gas field, Kashi Sag in Tarim basin. *Nat. Gas Geosci.* **2005**, *16*, 507–513. (In Chinese with English Abstract)
53. Wang, Z.; Zhao, M.; Zhang, S.; Song, Y.; Xiao, Z. A preliminary study on formation of Akemo gas field in the Kashi Sag, Tarim basin. *Chin. J. Geol.* **2005**, *40*, 237–247. (In Chinese with English Abstract)
54. Leach, D.L.; Sangster, D.F.; Kelley, K.D.; Large, R.R.; Garven, G.; Allen, C.R.; Gutzmer, J.; Walters, S. Sediment-hosted lead-zinc deposits: A global perspective. *Econ. Geol.* **2005**, *100*, 561–607.
55. Chen, J.; Wang, B.; Guo, X.; Cao, Z.; Liu, Y.; Geng, F.; Zhang, X.; Xu, H.; Zhao, J. Application of laser in-situ U-Pb dating of calcite to determination of the absolute time of hydrocarbon accumulation in polycyclic superimposed basins: A case study on Tahe oilfield, Tarim basin. *Oil Gas Geol.* **2021**, *42*, 1365–1375. (In Chinese with English Abstract)
56. Lv, X.; Shi, S.; Yang, W.; Hu, H.; Maihemuti, D.; Li, S.; Zhu, X. The key ore-controlling factors of the Wulagen superlarge Zn-Pb deposit, Xinjiang, China. *Miner. Explor.* **2021**, *12*, 900–909. (In Chinese with English Abstract)
57. Saintilan, N.J.; Spangenberg, J.E.; Chiaradia, M.; Chelle-Michou, C.; Stephens, M.B.; Fontboté, L. Petroleum as source and carrier of metals in epigenetic sediment-hosted mineralization. *Sci. Rep.* **2019**, *9*, 1–7. [[CrossRef](#)] [[PubMed](#)]
58. Sanz-Robinson, J.; Williams-Jones, A.E. Zinc solubility, speciation and deposition: A role for liquid hydrocarbons as ore fluids for Mississippi Valley Type Zn-Pb deposits. *Chem. Geol.* **2019**, *520*, 60–68. [[CrossRef](#)]
59. Migdisov, A.A.; Guo, X.; Williams-Jones, A.E.; Sun, C.J.; Vasyukova, O.; Sugiyama, I.; Fuchs, S.; Pearce, K.; Roback, R. Hydrocarbons as ore fluids. *Geochem. Perspect. Lett.* **2017**, *5*, 47–52. [[CrossRef](#)]